Pergamon

Gibbsite growth kinetics on gibbsite, kaolinite, and muscovite substrates: Atomic force microscopy evidence for epitaxy and an assessment of reactive surface area

Kathryn L. Nagy,[1,*,†] Randall T. Cygan,[1] John M. Hanchar,[2,‡] and Neil C. Sturchio[2]

[1]Geochemistry Department, Sandia National Laboratories, Albuquerque, Mew Mexico 87185-0750, USA
[2]Environmental Research Division, Argonne National Laboratory, Argonne, Illinois 60439-4843, USA

Abstract—New experimental data for gibbsite growth on powdered kaolinite and single crystal muscovite and published data for gibbsite growth on gibbsite powders at 80°C in pH3 solutions show that all growth rates obey the same linear function of saturation state provided that reactive surface area is evaluated for each mineral substrate. Growth rate (mol m^{-2} s^{-1}) is expressed by Rate$_{ppt}$ = (1.9 ± 0.2) × 10^{-10}|ΔG_r|/$RT^{(0.90 \pm 0.01)}$, which applies to the range of saturation states from ΔG_r = 0 to 8.8 kJ mol^{-1}, where ΔG_r = $RT[\ln(Q/K)]$ for the reaction Al^{3+} + 3H$_2$O = Al(OH)$_3$ + 3H$^+$, and equilibrium defined as ΔG_r = 0 was previously determined. Identification of the growth phase as gibbsite was confirmed by rotating anode powder x-ray diffraction. Rates on kaolinite were determined using steady-state measured changes between inlet and outlet solutions in single-pass stirred-flow experiments. Rates on muscovite were determined by measuring the volume of precipitated crystals in images obtained by Tapping Mode™ atomic force microscopy (TMAFM). In deriving the single growth rate law, reactive surface area was evaluated for each substrate mineral. Total BET surface area was used for normalizing rates of gibbsite growth onto powdered gibbsite. Eight percent of the BET surface area, representing the approximate amount occupied by the aluminum octahedral sheet exposed at crystal edges, was used for powdered kaolinite. The x - y area of the TMAFM images of the basal surface was used for single crystal muscovite. Linearity of growth rates with saturation state suggests that the dominant nucleation and growth mechanisms are two dimensional. Such mechanisms are supported by observations of the morphologies of gibbsite crystals grown on muscovite at ΔG_r = 8.8 kJ mol^{-1}. The morphologies include (1) apparent epitaxial films as determined by hexagonal outlines of edges and thicknesses of 30 to 40 Å, (2) elongate crystals 30 to 40 Å thick aligned with the structure of the distorted Si-tetrahedral sheet of the 2M_1 muscovite, and (3) micrometer-scale three-dimensional clumps of intergrown crystals. Reactive surface area as defined now for heterogeneous crystal growth in reactive-transport models must be modified to include substrates other than that of the growing mineral and to account for the role of structural and chemical controls on epitaxial nucleation and growth. *Copyright © 1999 Elsevier Science Ltd*

1. INTRODUCTION

Reactive-transport models for ground water and soil systems (Lichtner et al., 1996) recently have become more sophisticated in their ability to handle more complex kinetic reactions for dissolution and growth. Important remaining constraints in successful application of such models include issues such as how to describe coupled reactions and flow in unsaturated systems and the lack of rate laws that accurately describe reactions of Si- and Al-bearing minerals as they occur in nature. In particular, our understanding of reactive surface area is limited (White and Peterson, 1990). Also, little attention has been paid to accurate modeling of nucleation and growth reactions of secondary layered silicates, a common product of primary mineral dissolution reactions. As an example, Steefel and Van Cappellen (1990) used a classic rate law for homogeneous nucleation and growth to simulate the growth of halloysite in a bauxite. Subsequent formation of kaolinite in their model took place by heterogeneous nucleation and crystal

growth on existing kaolinite and on the metastable halloysite. More typically, heterogeneous growth is assumed to occur only on seeds of the growing mineral initially present in the system and at an arbitrary supersaturation above which growth begins on this surface.

One questionable assumption in reactive-transport modeling is that for supersaturations near equilibrium a mineral will grow only on itself. Steefel and Van Cappellen (1990) addressed this in part by allowing kaolinite to grow on precursor kaolinite as well as on halloysite. Nature, however, teems with examples of topotactic and epitaxial mechanisms of heterogeneous nucleation and growth of sheet-structured minerals on dissimilar phases including organic surfaces (e.g., Hochella and Banfield, 1995; Barker and Banfield, 1996; Fortin et al., 1997; Charlet and Manceau, 1994; Nugent et al., 1998). There is observational evidence from soils and sedimentary rocks that kaolinite grows epitaxially on the basal surfaces of detrital and secondary sheet silicates (e.g., Merino et al., 1993; Crowley, 1991; Pevear et al., 1991), kaolinite grows epitaxially on the edges of weathered montmorillonites (Altschuler et al., 1963), and that Mg-smectites nucleate on basal surfaces of detrital clays in alkaline lakes (Banfield et al., 1991a, 1991b). Numerous data from the soils science literature show that the extent of crystalline Al-hydroxide formation is controlled by the presence of clay mineral substrates (Jardine and Zelazny, 1996). Despite

---

*Author to whom correspondence should be addressed (kathryn.nagy@colorado.edu).
† *Present address:* University of Colorado at Boulder, Department of Geological Sciences, Boulder, Colorado 80309-0399, USA.
‡ *Present address:* Department of Geology, The George Washington University, Washington, D.C. 20052, USA.

these data, there has been no quantitative measure of how the kinetics of nucleation and growth of Al and Si-bearing phases are affected by substrates. Chiarello and Sturchio (1994) have addressed this general problem in a recent study on carbonates using synchrotron radiation to examine epitaxial growth rates of otavite on the (1014) calcite cleavage surface. In the present study we ask two questions. First, do the growth kinetics of a sheet-structured mineral on other sheet-structured minerals vary from substrate to substrate? Second, how can we more accurately assess the definition of reactive surface area with respect to growth of sheet-structured minerals in reactive-transport models?

Growth rates of gibbsite at 80°C obtained previously (Nagy and Lasaga, 1992; 1993) have been combined with new data for growth of gibbsite on powdered kaolinite and on single crystal muscovite to formulate a single growth rate for gibbsite that takes into account reactive surface area of the mineral substrates. The gibbsite precipitate on kaolinite was identified using rotating anode powder x-ray diffraction and its growth morphology on muscovite was determined using Tapping Mode™ atomic force microscopy (TMAFM). In addition, we used a new method for measuring growth rate volumetrically from TMAFM images. Growth rates of gibbsite on sheet-hydroxide and sheet silicate surfaces follow the same linear function of saturation state when normalized to either BET or well-defined geometric surface areas, and when the role of edge versus basal surfaces is considered. If growth rates are to be normalized to seed mineral surface areas in reactive-transport models, then at the very least, structurally similar phases that are present in the system must be considered as potential nucleation and growth surfaces.

2. METHODS

2.1. Solids

Experiments were conducted on powdered kaolinite with a size range of 0.15–0.4 μm (Twiggs Co., Georgia, see Nagy and Lasaga, 1993 and Nagy et al., 1991 for descriptions) and on ~1.44 cm^2 pieces of single crystal muscovite. The N$_2$ BET surface area of the kaolinite is 21.8 m^2 g^{-1}. Surface areas at the end of the experiments were within 10% of this value, the standard error associated with a BET analysis. The muscovite was obtained from Ted Pella, Inc. and is referred to as Agar muscovite. It is a nearly pure K$_2$Al$_4$(Si$_6$Al$_2$)O$_{20}$(OH)$_4$ mica with trace Fe as determined by Rutherford backscattering spectroscopy and has a $2M_1$ structure as determined by single crystal electron diffraction. A single crystal fragment was mounted on a Siemens P4 diffractometer equipped with an 18 kW, Mo rotating-anode generator operating at 50 KV and 250 Ma. Unit cell parameters were determined using 24 low-angle reflections in each of positive and negative 2θ space according to the method described in Smyth et al. (1997). Agar muscovite was obtained as single sheets one inch square and 0.03 mm thick. These sheets were cut into four pieces, each about 1.2 cm square, using a sharp, clean, single-edged razor blade. The pieces were cleaned of small particles created during the cutting process by blowing compressed gas at the surface. Cleaning was also conducted by cleaving each piece of muscovite with adhesive tape to expose a fresh basal surface, paying special attention to lightly touching the edges to pick up remnant particle flakes. The geometric surface area of each muscovite crystal was approximately 2.5 m^2 g^{-1}. The proportion of edge to basal surface was <5%.

2.2. Solutions

Inlet solutions were composed of 0.001 M Al(NO$_3$)$_3$ spectroscopic grade standard solutions with measured pH adjusted to slightly greater

than 3 using HCl. Inlet and outlet concentrations of Al, Si, and K (in the case of muscovite) were measured using a SpectraSpan 7 direct-current argon plasma (DCP) spectrometer and spectroscopic standard solutions. The pH was measured at 80°C, using Ross combination glass pH electrodes calibrated with Na-phosphate and KH-pthalate buffers (Bates, 1973), with the exception of the outlet pH for experiment KG2, which was calculated using the thermodynamic model based on the decrease in Al concentration.

Solution saturation states were calculated using the same thermodynamic model described in Nagy et al. (1991) and Nagy and Lasaga (1992), and were based on steady-state outlet solution compositions. The aluminum thermodynamic data were obtained from the work of Palmer and Wesolowski (1992) and Wesolowski (1992) on gibbsite solubility. The gibbsite solubility determined in the kinetic study of Nagy and Lasaga (1992) falls on the solubility curve determined by a reanalysis of all published experimental data in the aqueous aluminum system (e.g., Fig. 2 of Pokrovskii and Helgeson, 1995). The calculated error in saturation state (shown in Fig. 1) is based on the standard errors of the Al and pH analyses (see Nagy and Lasaga, 1992). Any minor inaccuracy in Al thermodynamic data would result in the same relative shift in position of all calculated saturation states and would not change the mathematical form of the rate equation (e.g., Burch et al., 1993). In experiments using the muscovite substrate, outlet solution compositions were not measurably distinct from inlet solution compositions reflecting the low total surface area available for nucleation and growth of gibbsite and for dissolution of muscovite.

2.3. Experiments

Experiments were conducted in stirred-flow reactors. A reaction vessel similar in design to those described by Nagy et al. (1991) was used for the kaolinite powder experiments. For the single crystal experiments, the reaction vessel was modified to separate the muscovite sheet from the underlying stir bar. A fritted plastic disk was added to the cell to compartmentalize the ~45 mL interior reaction chamber. The fluid flowed into the lower stirring compartment and then into the upper compartment containing the muscovite. The crystal again was freshly cleaved with adhesive tape 2 to 3 times on each side immediately prior to placing it in a reactor nearly filled with inlet solution. The reactor was sealed and placed in an 80°C water bath. The muscovite crystal was large enough to not turn over during the experiment although it was free to move up and down slightly in response to the force of the upward fluid flow. At times the bottom-facing muscovite surface appeared to lie on the fritted divider; however, the upward flow was fast enough to maintain the muscovite in a floating configuration the majority of the time.

Powder experiments were dismantled according to previous practices (Nagy et al., 1991). For single crystal experiments, drying was accelerated by blowing the crystal surface gently from about a 12″ distance with a compressed gas. This was done to avoid precipitation of additional material onto the surface as the solution evaporated. Such material was generally observable with a binocular or atomic force microscope and appeared as rings of crystals that formed at the edge of a slowly drying droplet. In SEM images, such precipitates were large, thick particles with irregular edges and intraparticle cracks. This type of precipitate morphology was avoided in the AFM analysis described below. Identity of the "up" and "down" sides of the muscovite single crystal was maintained during subsequent surface analysis.

2.4. Atomic Force Microscopy

Gibbsite crystallites on muscovite single crystal surfaces were examined in air using a Digital Instruments (DI) Multimode Nanoscope IIIa in Tapping Mode™ (TMAFM) with silicon tips from DI. The crystal was cut in half perpendicular to the basal plane. Each piece was used to examine one of the two exposed basal surfaces of the original crystal. Care was taken to not touch the crystal prior to mounting on a metal disk. Scanned areas were a maximum of 12 μm × 12 μm, and were obtained using the E scanner head of the DI instrument, which has a z-dimension range of 2.5 μm. The volume of precipitate on the basal surface within a 144 μm^2 imaged area was determined using the "bearing analysis" program within the DI image analysis software. This program calculates the volume of material above a selected base height
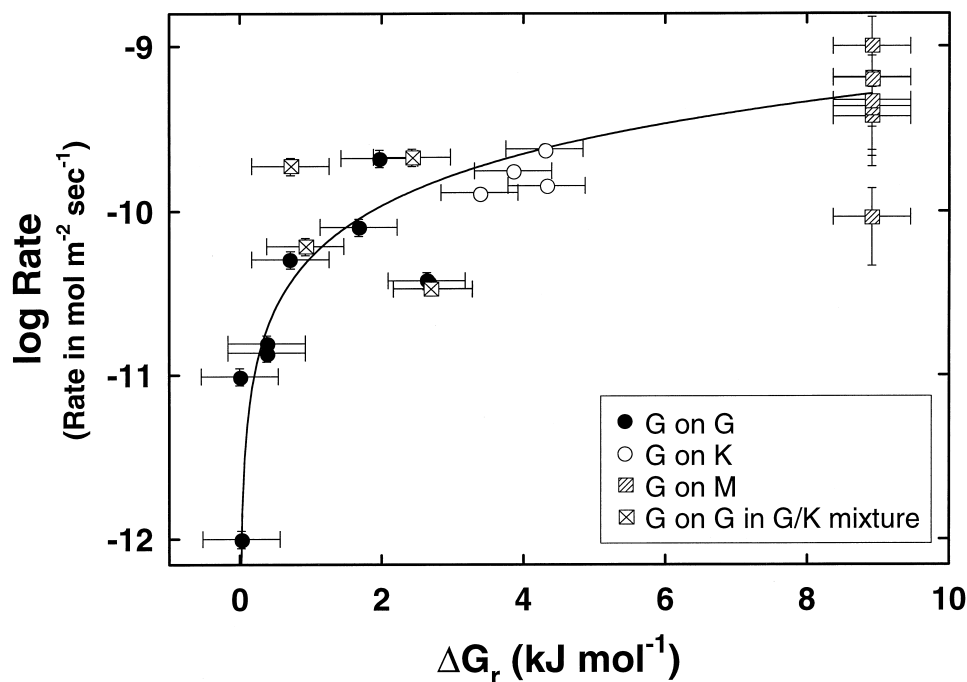
Fig. 1. Gibbsite growth rates on gibbsite, kaolinite, and muscovite as a function of solution saturation state at 80°C and pH3. The curve is fit through all data and given by Eqn. (2). The growth rates on gibbsite are normalized to total BET surface area, on kaolinite to 8% of the BET surface area, and on muscovite to the basal surface area imaged using TMAFM. G on G refers to gibbsite growth rates on gibbsite powders (Nagy and Lasaga, 1992); G on K refers to gibbsite growth rates on kaolinite powders (this study); G on M refers to gibbsite growth rates on muscovite single crystals (this study); and G on G in G/K mixture refers to gibbsite growth rates on gibbsite in a mixed gibbsite and kaolinite powder (Nagy and Lasaga, 1993).

within the image by integrating under the three-dimensional curve (the Z or height data in the digital image) that defines the surface topography. Each entire 144 μm^2 image was selected and the average darkest (topographically lowest) area was assumed to represent the muscovite surface.

The relative orientations of one type of gibbsite crystal (the elongated crystals discussed in the results section) were measured from one TMAFM image and plotted on a Rose diagram in order to assess the potential epitaxial control of the muscovite substrate on the nucleation and growth of the gibbsite.

2.5. Growth Rate Calculations

Growth rates from powder experiments were calculated according to the steady-state decrease in Al measured in the outlet solutions according to Eqn. (12) in Nagy and Lasaga (1992). The initial BET surface area of the kaolinite was used to normalize the rates. To obtain the overall gibbsite growth rate law we used 8% of the initial BET surface area which is the approximate amount of edge surface area of the aluminum dioctahedral sheet (see Sec. 4). Error in rate is ±12% and is controlled largely by the uncertainty of a BET surface area measurement (Nagy and Lasaga, 1992).

Rates from single-crystal experiments were calculated using the volume of precipitate determined by the image analysis software normalized to the original 144 μm^2 geometric area of the basal surface of the muscovite. The volume was converted to moles of gibbsite and normalized to the experimental duration to arrive at a rate expressed in units of mol m^{-2} s^{-1} for comparison with the powder experiments. Rates were obtained from both sides of each single crystal. Because the larger crystal clumps do not represent a solid column of material above the surface, but rather a column with void space due to the interlocking array of crystals, the total calculated volume of material must be too high. We have estimated that up to 50% of the integrated volume may be void space based on a visual assessment of the crystal clumps. This

would result in an overestimate of rate by no more than 50%. However, the volume of smaller crystals may be hidden in the noise of the image; i.e., the background baseline which is represented by the darkest area of the image may be incorrectly selected. If small crystals on the order of 1 unit cell in thickness (10 Å high) covered the surface and were not counted in the analysis, the rate would be underestimated by approximately 10%. Also, in comparison to rates on powdered substrates, rates on muscovite substrates might be less because only one crystallographic surface, the basal surface, is considered. We did not measure growth on the muscovite edges. Variability in reported rates from one experiment also may arise from the small area sampled for any one rate analysis using this technique. If the precipitation of gibbsite on the basal surface of muscovite is not uniform at this scale, less precision in rates is expected.

2.6. Computational Simulations

Atomic-scale details of the muscovite structure were simulated in order to explain the patterns of gibbsite crystal shapes and orientations observed using TMAFM. The computational model is based on obtaining an energy-minimized configuration of hard-sphere atoms based on a simple interatomic potential. The potentials are obtained from *ab initio* molecular orbital calculations of cation-oxygen clusters (Collins and Catlow, 1990) that were then fit to an interionic energy expression that includes a simple 6–12 Lennard-Jones function:

$$E = \sum_{ij} \frac{q_i q_j}{r_{ij}} + \sum_{ij} \left(\frac{A_{ij}}{r_{ij}^{12}} - \frac{B_{ij}}{r_{ij}^6} \right). \qquad (1)$$

The total energy of the system (lattice energy E) is evaluated as a function of the interatomic distances r_{ij} where q_i and q_j are the ionic charges and A_{ij} and B_{ij} are the fitted potential parameters. The $1/r^{12}$ term represents the positive short-range repulsion of interacting ions,

Table 1. Calculated parameters at steady-state for all experiments in which gibbsite precipitated onto kaolinite (KG) and muscovite (MG) at 80°C and pH3.

Expt. no.	$M_{Al^{3+}}$ (μmol L^{-1})	$\log(a_{Al^{3+}}/a_{H^+}^3)$	ΔG_r (kJ mol^{-1})	Rate (mol m^{-2} s^{-1})
KG1	670	5.50	3.381	1.0×10^{-11}
KG2	637	5.64	4.297	1.9×10^{-11}
KG19	664	5.57	3.853	1.4×10^{-11}
KG20	692	5.64	4.326	1.1×10^{-11}
MG1 up*	603	6.38	8.912	6.4×10^{-10}
MG1 down	603	6.38	8.912	9.2×10^{-11}
MG3a up	603	6.38	8.912	4.7×10^{-10}
MG3b up	603	6.38	8.912	4.3×10^{-10}
MG3c up	603	6.38	8.912	3.8×10^{-10}
MG3d down	603	6.38	8.912	1.0×10^{-9}
MG3e down	603	6.38	8.912	6.5×10^{-10}

* Up refers to the side of the muscovite single crystal that faced the top of the reactor; down refers to the side facing down and receiving the upward force of the flow. MG1 and MG3 refer to two different experiments. The designations a, b, etc., refer to different imaged areas of the same 144 mm^2 surface.

while the $1/r^6$ term is for the attractive van der Waals energy. Note that due to the large exponent values in the denominators of the second summation terms, these energy contributions are significant at only very short distances (1 to 2 Å). In contrast, the lattice energy in an ionic model is dominated by the long-range electrostatic or Coulombic interactions, i.e., the first term in Eqn. (1). With the energy varying as $1/r$, the electrostatic term is more difficult to evaluate for a periodic crystalline phase. An Ewald summation method provides fast convergence for the Coulombic term by evaluating part of the energy summations in reciprocal space (Tosi, 1964).

An idealized structure for the muscovite was constructed based on its stoichiometry. Aluminum was substituted randomly so that one atom was sited in each of the two tetrahedral layers of the unit cell. Four different configurations for the aluminum positions were selected in order to treat the order–disorder expected in muscovite. Although, the muscovite unit cell is monoclinic, we converted the unit cell to P1 symmetry to ensure a fully optimized configuration for atomic positions and cell parameters as influenced by the tetrahedral site disorder. Ions were assigned full unit charges q_i corresponding to their formal valence charge.

The forcefield energy program Discover (Molecular Simulations, Inc.) was used to compute the total energy for the atomic configuration, and then all atom positions and unit cell parameters were allowed to

vary using a conjugate-gradient energy-minimizer algorithm. Typically, the muscovite structure was completely relaxed to an optimized structure within 50 iterations.

RESULTS

3.1. Rates

Rates calculated for four powder and two single crystal experiments are listed as a function of solution saturation state expressed as ΔG_r in Table 1. Seven rates are reported for the single crystal experiments, representing data obtained from different areas on both basal surfaces of each muscovite crystal. Table 2 includes additional pertinent experimental information. The eleven new rates are included with eleven previously published rates for gibbsite growth on gibbsite powders (Nagy and Lasaga, 1992) and gibbsite growth on gibbsite in mixed gibbsite and kaolinite powders (Nagy and Lasaga, 1993) in Fig. 1. Note that the rates for gibbsite growth on kaolinite shown in Fig. 1 were normalized to 8% of the kaolinite's BET surface

Table 2. Experimental parameters for gibbsite precipitation experiments at 80°C and pH3.

Expt. no.	Input Al (μmol L^{-1})	Input pH	Output Al (μmol L^{-1})	Output pH	I (mol L^{-1})	Starting mass (g)*	Flow rate (mL min^{-1})	Duration (da)
KG1	1028	3.30	857	3.02	0.00563	0.7279	0.0577	27.1
KG2	1028	3.30	777	2.95**	0.00557	0.7316	0.0517	13.3
KG19	1022	3.35	853	3.00	0.00558	0.7670	0.0849	16.8
KG20	1022	3.30	887	3.02	0.00577	0.7583	0.0840	23.8
MG1 up#	1000†	3.29	1000	3.04	0.00514	NA§	0.155	46.9
MG1 down	1000†	3.29	1000	3.04	0.00514	NA	0.155	46.9
MG3a up	1000†	3.30	1000	3.04	0.00514	NA	0.155	7.12
MG3b up	1000†	3.30	1000	3.04	0.00514	NA	0.155	7.12
MG3c up	1000†	3.30	1000	3.04	0.00514	NA	0.155	7.12
MG3d down	1000†	3.30	1000	3.04	0.00514	NA	0.155	7.12
MG3e down	1000†	3.30	1000	3.04	0.00514	NA	0.155	7.12

* Surface area of kaolinite = 21.08 m^2 g^{-1}; surface area analyzed in each muscovite experiment = 1.44×10^{-10} m^2.

** Calculated.

Up refers to the side of the muscovite single crystal that faced the top of the reactor; down refers to the side facing down and receiving the upward force of the flow.

† Difference between input and output solutions for muscovite experiments was immeasurable due to the relatively low total surface area of the substrate.

§ Not applicable.

area. This amount of reactive surface area corresponds to a reasonable estimate of edge surface area occupied by the aluminum dioctahedral sheet (see discussion). The line in Fig. 1 was fitted to all data, and is expressed by

$$\text{Rate}_{\text{ppt}} = (1.9 \pm 0.2) \times 10^{-10} |\Delta G_r| / RT^{(0.90 \pm 0.01)}, \quad (2)$$

where Rate_{ppt} has units of mol m^{-2} s^{-1}. The equation applies for the measured range of saturation states from $\Delta G_r = 0$ to 8.8 kJ mol^{-1}, where $\Delta G_r = RT[\ln(Q/K_{\text{eq}})]$ for the reaction $Al^{3+} + 3H_2O = Al(OH)_3 + 3H^+$, and equilibrium defined as $\Delta G_r = 0$ was previously determined by Nagy and Lasaga (1992). (R is the gas constant, T is temperature in Kelvin, Q is the ion activity product in the disequilibrium solution, and K_{eq} is the equilibrium ion activity product.) If normalized to total BET surface area, the four rates on the kaolinite substrates (Table 1) are less than one tenth of the rates defined by the fitted curve.

Nagy and Lasaga (1992) chose two equations to describe gibbsite growth rate each of which is essentially a linear function of saturation state. We chose the simpler functional form for comparing all data in the present study. Equation (2) agrees well with the original rate equation for gibbsite growth on gibbsite seeds [Eqn. (15) of Nagy and Lasaga, 1992].

3.2. Growth Phase Identity

Although previous work (Nagy and Lasaga, 1992) relied primarily on indirect evidence for identifying the Al-bearing growth phase, i.e., the measured change in solution composition, we are able to prove that gibbsite is the phase that forms from the pH 3 supersaturated solutions at 80°C. This has been accomplished using rotating anode powder x-ray diffraction (XRD) (Fig. 2). Comparison of the amount of precipitate determined from XRD to the amount determined from quantitative solution chemistry changes is discussed in Hanchar et al. (1999). Typically, quantification of precipitate by the powder XRD technique yields amounts that are less than amounts determined by solution analysis. These differences are likely a result of the variation in precipitate grain size and the inability of the rotating anode XRD technique to detect small amounts of the smallest crystallites (on the order of one to a few unit cells in the c direction).

3.3. Growth Phase Morphology on the Muscovite Substrate

The crystallographic match of the gibbsite basal plane on the muscovite basal plane is expected to be close (Table 3). Therefore, quantifying the morphology of gibbsite crystallites on the muscovite single crystals should indicate the importance of epitaxial controls on growth.

At the highest supersaturations investigated, three types of crystal morphology are observed (Figs. 3–5). The first type is a large cluster of pseudo-hexagonal platelets that appear to be intergrown, perhaps on a twinning basis (Fig. 3). These clusters extend up to about 1 μm above the muscovite surface and are up to 2 μm in diameter. The second type of morphology is a micron-wide "thin film" (Fig. 4a). The films are 30 to 40 Å high and appear to be composed of small interlocking crystals all oriented with their basal planes parallel to the basal plane of
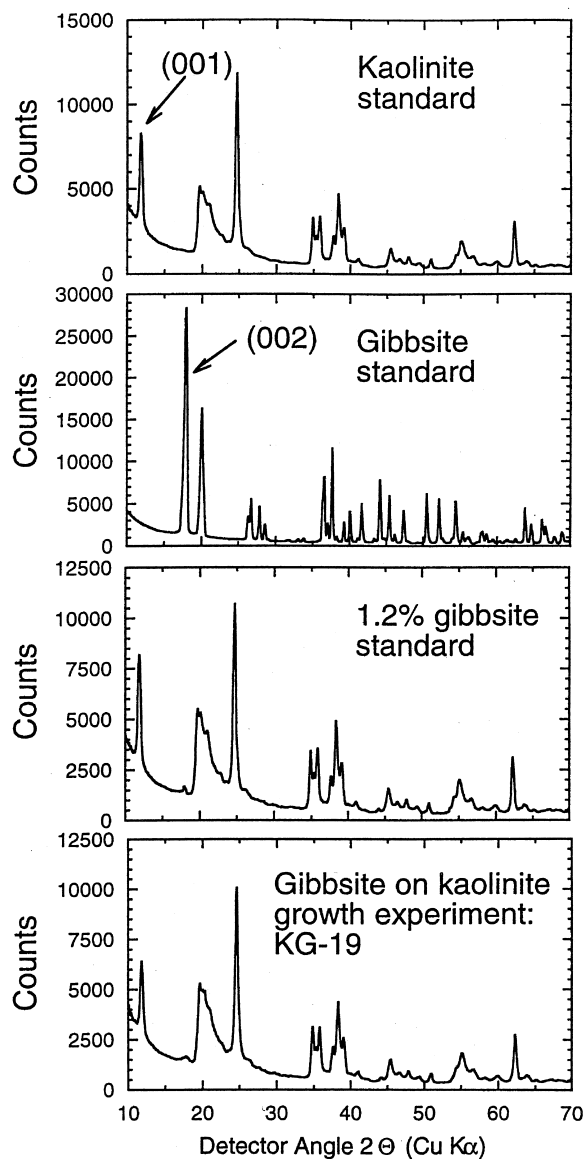

Fig. 2. Identification of gibbsite as the growth phase using rotating anode XRD. (a) Twiggs Co. Georgia kaolinite standard, (b) Alcoa gibbsite standard (substrated used in Nagy and Lasaga, 1992), (c) 1.2% Alcoa gibbsite in Twiggs Co. Georgia kaolinite, (d) expt. KG19 showing 1% gibbsite precipitated in Twiggs Co. Georgia kaolinite. The amount determined by XRD compares well with that determined from the steady-state change in solution composition in the stirred-flow reactor experiment.

muscovite. A closer look at the edge of a film (Fig. 4b) shows a detailed hexagonal outline that appears to mimic the near-hexagonal structure of the muscovite basal surface. The third type of morphology is a small elongated crystal approximately 30 to 40 Å high, 10 to 20 nm wide, and 50 to 80 nm long (Fig. 5a). The majority of this type of gibbsite crystallite is oriented in three dominant directions, which are also the directions of the hexagonal edges of the thin film areas. Two sets are oriented in opposite directions at 61°–68° and 50°–77° with respect to a third reference subset positioned at an arbitrarily

Table 3. Unit cell lengths for gibbsite, kaolinite, and muscovite.

Mineral	Formula	a(Å)	b(Å)	c(Å)	% misfit
Gibbsite	$Al(OH)_3$	8.684	5.078	9.736	0
Kaolinite	$Al_2Si_2O_5(OH)_4$	5.139	8.932	7.371	4.09
Muscovite[#,†]	$K_2Al_4(Al_2Si_6)O_{20}(OH)_4$	5.1895 (5)	9.0077 (8)	20.0482 (16)	5.85

* Gibbsite and muscovite are monoclinic. Kaolinite is triclinic. % misfit takes into account the triclinicity of kaolinite.

[#] $\beta = 95.779(7)°$; Vol. $= 932.40(13)Å^3$.

[†] Unit cell parameters determined in this study.

chosen orientation of 90° (vertically oriented crystallites in Fig. 5b).

3.4. Molecular Modeling Support for Epitaxial Growth on the Muscovite Basal Surface

The relative orientations of the small gibbsite crystallites and the hexagonal outlines of parts of the thin films suggest that the underlying crystallographic framework of the linked silicon tetrahedra of the muscovite epitaxially controls the nucleation and growth of gibbsite. We performed computer simulations using an ionic model of the bulk structure of muscovite in order to compare the tetrahedral sheet structure with the orientations of the gibbsite crystals on the muscovite basal surface. Using standard structural refinements of x-ray or electron diffraction

data, it is not possible to evaluate the exact distribution of siloxane bond angles associated with the (001) basal plane of the muscovite tetrahedral sheet. This is because the refinements involve averaging of the small variations in angles between Si-tetrahedra in the tetrahedral sheet. Further complications for the analysis are introduced by the isomorphic substitution of aluminum for silicon and related cation disordering on tetrahedral sites. Four different initial configurations of Al and Si are possible.

Figure 6 shows the local structure within the siloxane sheet from one of the four possible substitutional configurations. Two hexagonal rings are labeled with the six different O-O-O bond angles that are standard for evaluating the muscovite structure (e.g., see Bailey, 1984, p. 15). The range of O-O-O bond angles in Fig. 6 represents that observed in all four calculations. Half
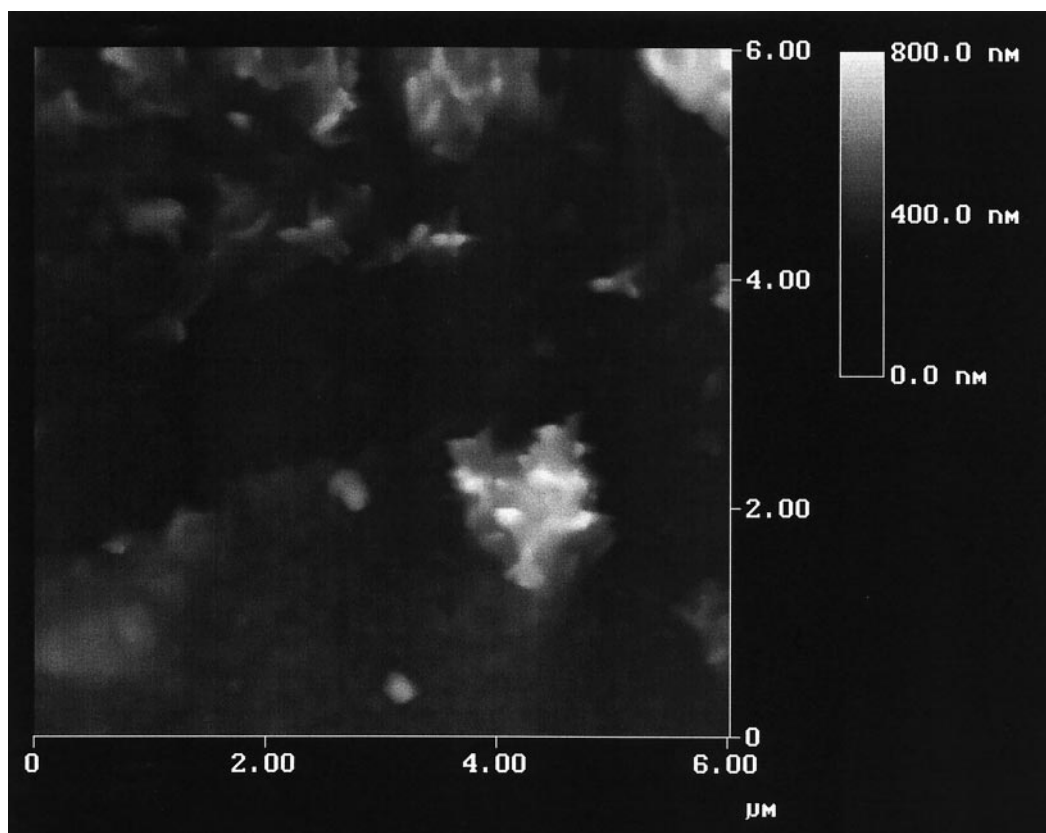

Fig. 3. TMAFM image of large clusters of intergrown gibbsite platelets on muscovite basal surface.
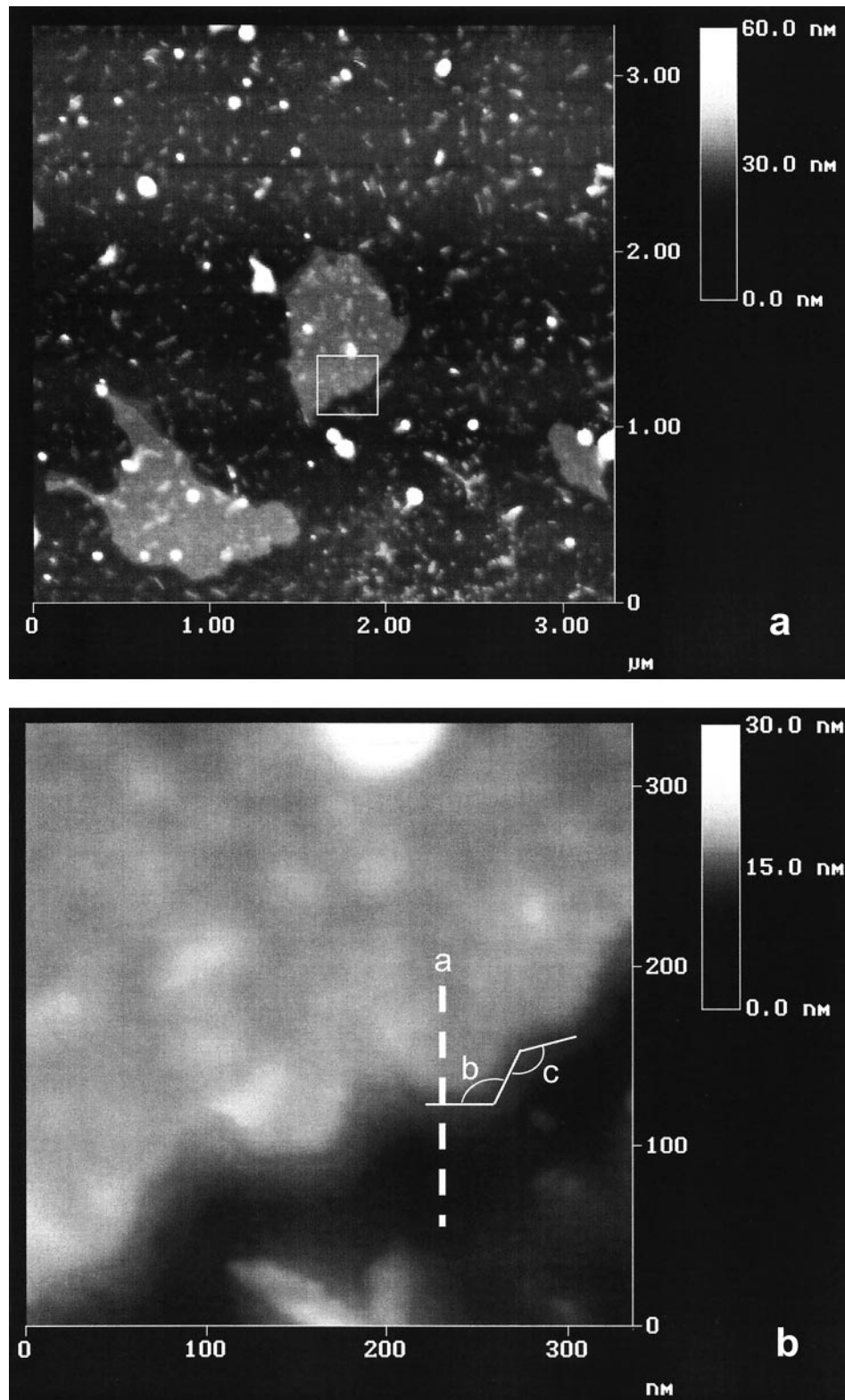
Fig. 4. (a) TMAFM image of "thin film" areas of precipitated gibbsite on muscovite basal surface. The figure also shows range of crystal morphology types. (b) Enlargement of the lower right edge of film shown in the white box in (a). Cross section of film marked "a" indicates a thickness of 40 Å. Edge of film has a hexagonal outline reflecting the underlying muscovite surface structure. Angles "b" and "c" are ~116° and ~140° (half-angle = 58° and 70°), respectively.
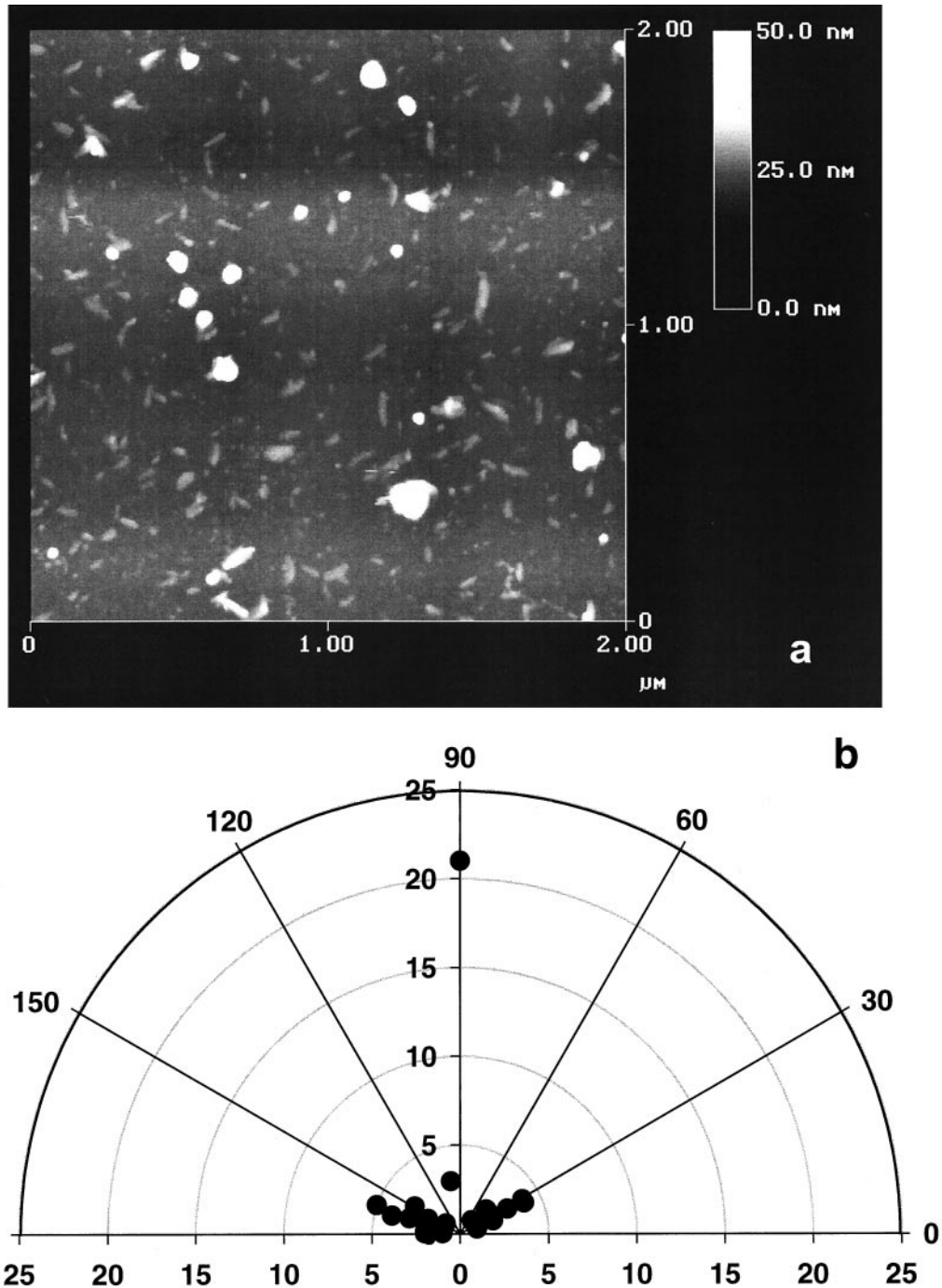
Fig. 5. (a) TMAFM image of gibbsite crystallites on muscovite basal surface demonstrating at least a bimodality in crystal size and an elongate morphology for the smaller oriented crystallites. (b) Rose diagram of relative orientations of the gibbsite crystallites. This diagram was determined by drawing lines along the edges of the elongate crystallites shown in (a) and measuring the angles of intersection between all lines. The vertically oriented crystals in (a) are plotted at 90°. The radial axis units are number of particles in a particular orientation.

angle values range from 49.5° to 70°. This range is in good agreement with the range of angles observed for the orientation of elongate crystallites of gibbsite on the muscovite surface (Fig. 3b). It is important to realize that the simulated siloxane sheet structure is derived from a bulk three-dimensional structure. In contrast, the TMAFM observations of gibbsite crystal-

lite orientation are related directly to the structure of the muscovite surface where additional distortion due to relaxation of the surface and near-surface atoms is expected. A valid simulation of the surface relaxation of muscovite is beyond the ability of the potential model used in this study due to the lack of an electronic polarization term.
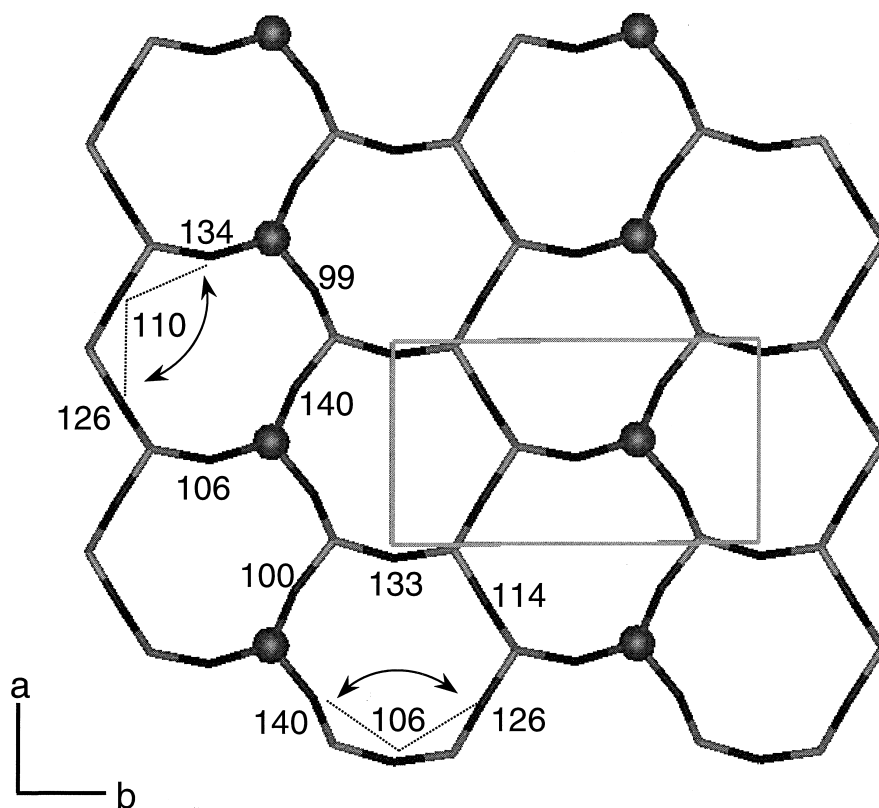
Fig. 6. Calculated local structure within the silicon-tetrahedral sheet of muscovite based on an empirical force field for describing ionic interactions within muscovite. Additional structural variation would be expected from a surface relaxation calculation. The light gray box represents the *a* (vertical) and *b* (horizontal) directions of the muscovite unit cell. Spheres represent aluminum atoms that substitute for silicon.

4. DISCUSSION

4.1. Gibbsite Growth Rate Law

The observation that gibbsite growth rates on gibbsite, kaolinite, and muscovite substrates can be expressed by a single rate law with a simple dependence on saturation state rests on a judicious evaluation of the reactive surface area that controls nucleation and growth in each case. In the following sections we evaluate possible controls exerted by the substrate minerals on nucleation and growth of gibbsite and explain how we estimated the proportion of reactive surface area for each of the substrates. Nucleation and growth of gibbsite depends on structural and chemical characteristics of the bulk substrates and their surfaces in addition to the saturation state of the solution.

4.2. Substrate Crystal Structure and Epitaxial Growth

A necessary condition for epitaxy is that some feature of the crystal structures of substrate and precipitate matches closely. Sheet-structured minerals share a similar arrangement of atoms on the basal planes and edge surfaces. The gibbsite structure is that of a "free" Al-octahedral sheet stacked in the *c* direction. In contrast, the Al-octahedral sheet in both kaolinite and muscovite is structurally distorted in order to bond to the tetrahedral sheets. In the *ab* plane, the octahedral sheet is stretched relative to the structure of the octahedral sheet in gibbsite. The crys-

tallographic misfit or degree of stretching between the basal planes of gibbsite and the three substrates increases in the order gibbsite < kaolinite < muscovite, where % misfit is calculated as the difference between the *ab* unit cell area of the mineral normalized to that of gibbsite (Table 3). To accommodate the stretching, the octahedral sheet in both kaolinite and muscovite is thinned relative to the "free" octahedral sheet of gibbsite. For both kaolinite and muscovite, the octahedral sheet is about 2.1 Å thick (Giese, 1988; Bailey, 1984) versus 2.425 Å thick in gibbsite (Taylor, 1987, p. 164). Thus, to have epitaxial growth on the basal planes of kaolinite and muscovite the gibbsite must be expanded in the *ab* plane by a maximum of approximately 6% in the case of muscovite. In contrast, to have epitaxial growth on the edge surfaces, the gibbsite sheet must be compressed by about 13% for muscovite and 14% for kaolinite. Considering the magnitude and relative sense of the structural misfits, it is probable that less energy is required for gibbsite to grow epitaxially on the basal surface of either substrate than on the edge surfaces, if the only control on growth is structural.

The elongated crystals formed on the basal surface of muscovite in experiments MG1 and MG3 show preferred orientations that reflect the structure of the silicon-tetrahedral layer. However, the measured angles between the crystals are slightly different from those derived from the $2M_1$ mica structure (Bailey, 1984, p. 15). Half values for the angles between apical

oxygens in the tetrahedral sheet of the averaged $2M_1$ structure are 68.5°, 56.05°, and 55.9°. These angles can explain some of the orientations observed, however not the breadth of the range. We showed that an energy-minimized bulk muscovite structure could explain the wider range of observed angles. Some deviation of the measured angles from the bulk averaged structure may indicate additional distortion of the surface tetrahedral sheet due to relaxation effects. For example, if K is decreased in the interlayer of muscovite, the *a* and *b* dimensions are shortened (Burns and White, 1963; Radoslovich and Norrish, 1962). The surface tetrahedral sheet exposed to solution may be slightly more distorted than a bulk structure tetrahedral sheet due to the lack of fixed K^+. Shortening of *a* and *b* does not have to change the angles between apical oxygens, but could decrease the % misfit between substrate and precipitating gibbsite. We were not able to measure K in the outlet solutions for these experiments, again because the total surface area available for reaction was low relative to our analytical detection limits.

Surface distortion may also arise from the polarizing effects of adsorbed water. Recently, data obtained by scanning polarization force microscopy were used to suggest that water condenses to form two-dimensional thin films with icelike structures depending on relative humidity that exhibit an epitaxial relationship with the muscovite basal surface (Hu et al., 1995). Odelius et al. (1997) simulated the structure of water on muscovite using first principles molecular dynamics calculations allowing for surface relaxation effects. The water molecules form a corrugated two-dimensional structure on the surface that encloses the K^+ ions. The corrugated hexagonal structure is reminiscent of the elongated crystal orientations observed in our TMAFM images.

Gibbsite growth should occur on all surfaces of gibbsite, although perhaps at different relative rates. Gibbsite substrate crystals are fairly equant in shape (Nagy and Lasaga, 1992), owing to their precipitation from basic solutions during Al-ore processing (e.g., Veesler and Boistelle, 1994). Gibbsite precipitated homogeneously from acidic solutions grows faster parallel to *a* and *b* than to *c*, and tends to form as thin hexagonal plates (Smith and Hem, 1972). We initially expected that gibbsite growth rates on kaolinite would be similar to those on muscovite due to similar geometric effects, if not slightly faster because of the smaller degree of misfit and because one entire basal surface of kaolinite is an Al-octahedral sheet. Previous work in which gibbsite was grown on mixtures of gibbsite plus kaolinite, suggested that gibbsite does grow faster on itself than on kaolinite (Nagy and Lasaga, 1993) by at least an order of magnitude. Therefore, we expected that growth rates on muscovite would be slower by a similar amount.

Contrary to our expectations, the data show that gibbsite growth rates on gibbsite and muscovite are similar, but on kaolinite are significantly slower. In order to understand this observation, we must consider other effects besides geometric ones. These effects include defect density, solution saturation state effects, characteristic permanent charge arising from isomorphic substitutions, and pH-dependent surface charge.

4.3. Effects of Defect Density, Saturation State, and Surface Charge Density

In general, crystal growth theories state that heterogeneous nucleation is preferred over homogeneous nucleation because the free energy barrier is reduced in the presence of a surface. The specific nucleation and growth mechanism depends on the saturation state of the solution as well as microstructure and surface charge characteristics of the substrate. For example, nucleation and growth may occur at spiral dislocations (Burton et al., 1951) or as isolated islands which grow outward at their edges ("birth and spread model", Ohara and Reid, 1973), and specific regions of supersaturation may favor one mechanism over the other (e.g., Teng et al., 1998). Although the experiments of this study were conducted over a range of saturation states and with different substrate minerals, comparative evaluations of defect density, solution saturation state, and surface charge effects on the growth rates are possible. These lead to an inference that surface charge density and type determine the gibbsite nucleation sites on kaolinite and muscovite. Subsequent growth does not occur as monolayer coverage but rather by a variety of mechanisms that may reflect the relatively high supersaturations investigated.

4.3.1. Substrate defect density and solution saturation state

If the lower rates of gibbsite growth on kaolinite when normalized to total BET surface area were a function of microstructural or chemical defect density, it would be necessary for kaolinite to have ≤10% of the defect density of the gibbsite and muscovite. We did not measure defect density in the three substrate minerals. However, we can argue against a lower defect density in the kaolinite substrate relative to the muscovite and gibbsite substrates for the following reasons.

First, the kaolinite is a poorly crystallized kaolinite as indicated by its Hinckley index of 0.52 (an XRD measure of crystallinity) (Nagy et al., 1991). Structural models of kaolinites relate the Hinckley index to concentrations of structural defects (stacking faults) including layer translations and rotations, and random displacements of the vacant octahedral sites (Giese, 1988), and a low Hinckley index corresponds to a relatively high defect density. Sedimentary or soil kaolinites also commonly contain chemical defects that might generate high-energy nucleation sites (Muller et al., 1995). Second, the muscovite likely has a low defect density because it was optically clear, nearly chemically pure, and could be cleaved to produce atomically smooth surfaces over large areas many millimeters wide as determined by extensive experience imaging the muscovite using AFM. Any dislocations intersecting the muscovite basal surface would typically produce rare steps easily visible in reflected light on the basal surface or in AFM images. A high dislocation or chemical defect density also would have been expected to alter the translucence of the crystals. Third, the presence of dislocations has been proposed to explain rapid increases in the dissolution rate of gibbsite with a critical bulk solution ΔG_r value (Nagy and Lasaga, 1992) resulting in a nonlinear relationship between rate and saturation state. The growth rates of gibbsite on gibbsite overlap in saturation state space with the growth rates on kaolinite (Fig. 1). However, the gibbsite growth rates on gibbsite by them-

selves define a linear relationship to saturation state. This suggests that the growth mechanism on the gibbsite substrate is not controlled by dislocation defects, which in turn implies that the defect density of gibbsite is not high.

It is likely that kaolinite has the highest structural and chemical defect density based on its poorly crystallized nature. Therefore, if defect density controls nucleation site density, kaolinite should have the most nucleation sites resulting in faster gibbsite growth rates. This directly contrasts with the observation that growth rates on kaolinite were observed to be slower than on gibbsite or muscovite, and suggests that some other surface characteristic exerts the dominant control on nucleation and growth.

4.3.2. Permanent charge and electrostatic interactions

Neutralization of permanent charge through electrostatic binding of cations provides a mechanism that can explain a lower activation energy barrier for nucleation on muscovite than on kaolinite. Muscovite has a permanent structural charge arising from isomorphic substitution of Al for Si in the tetrahedral sheets. In a nearly pure $2M_1$ K-muscovite, this charge is close to -2 equivalents per formula unit [written using $O_{20}(OH)_4$], and is satisfied by interlayer K^+. Georgia kaolinites have at most a very small percentage of permanent structural charge (Brady et al., 1996), although the origin of this charge may be mineral inclusion or structural defects rather than isomorphic substitutions (Muller et al., 1995). Boles and Johnson (1983) suggested that the permanent charge of mica surfaces may control the precipitation of carbonate phases between the layers through the exchange of K^+ for H^+. Johnsson et al. (1992) proposed that exchange of K^+ for H^+ on the muscovite basal surface when immersed in acidic solutions may induce Al-hydroxide polymerization. In acidic solutions, aqueous Al^{3+} or $Al(OH)^{2+}$ may exchange for K^+ directly in one of every three or two charged sites, respectively. Similarly, Barnhisel (1969) had described precipitation of positively charged hydroxy Al polymers in the interlayers of montmorillonite as a mechanism of neutralizing permanent negative charge.

Regardless of the exact nature of the nucleation mechanism and subsequent bonding between gibbsite and muscovite, the morphology of the thin films supports polymerization of Al-units into octahedral sheets parallel to the muscovite basal surface. Both thin films and elongated crystals likely would be strained for some distance outward from the interface due to the structural misfit between gibbsite and muscovite. The structural misfit also may control the actual shape of the elongated crystals which contrasts with the hexagonal shape of crystals grown directly from solution (Smith and Hem, 1972). An alternative explanation for the elongated shape may be related to the formation of polynuclear Al complexes. Al_{13} polynuclear units form linear clusters ~400 Å in diameter from $AlCl_3$ solutions neutralized with NaOH (Bottero et al., 1987). Aging of aggregated Al_{13} polynuclear units produced elongated platelets ~550 Å long and 25 Å thick, and eventually longer particles up to 45 Å thick (Bottero et al., 1987). Perhaps chemical conditions at the muscovite/water interface are appropriate for the formation of polynuclear Al complexes from our experimental solutions.

Our observations of morphology are similar to those made earlier by Johnsson et al. (1992) of precipitates of undetermined composition formed upon reaction of the muscovite basal surface in distilled water in equilibrium with the atmosphere (pH = 5.7) at 22°C for 10 days. Using AFM, they observed small fiber-like structures after 2 days that expanded into film-like areas after 10 days. Their images (Johnsson et al., 1992, Fig. 3a), show fibers approximately 100–300 nm long with a width-to-length aspect ratio of 0.1–0.2. All of their surface precipitate features were about 10 Å high, the height of one unit cell of gibbsite, whereas our thin film areas and elongate crystals were 30–40 Å high. Harsh et al. (1984) observed using TEM that Al-hydroxide precipitated in the interlayers of montmorillonite formed rounded islands about 150 Å in diameter, comparable to the width of the elongate gibbsite crystallites that formed on muscovite outer surfaces in this study.

4.3.3. pH-dependent surface charge

Protonated Al-sites, with surface densities that are pH-dependent for the three substrate minerals, could act as preferential docking points for aqueous Al species. At 25°C and pH3, aluminum edge sites of kaolinite are highly protonated and more acidic than hydroxylated sites on either the octahedral or tetrahedral surface (Brady et al., 1996). The acidity of these edge sites decreases slightly with an increase in temperature to 70°C. Muscovite edges should be protonated similarly to kaolinite at pH3. This assertion is supported by comparing the experimentally determined pH_{ZPC} (zero point of charge) for kaolinite of 4.5 (Carroll-Webb and Walther, 1988) with the calculated pH_{PPZC} (pristine point of zero charge) values for kaolinite (4.66) and muscovite (6.6) of Sverjensky (1994) all at 25°C. Gibbsite, on the other hand, is highly protonated at pH3 (pH_{ZPC} and pH_{PPZC} ~10) (Sverjensky, 1994). The hexagonal platelike morphology of gibbsite formed in acidic solutions (Smith and Hem, 1972) indicates that on gibbsite, aluminol edge sites also appear to be the more reactive sites for growth.

Jardine and Zelazny (1996) reviewed the literature on adsorption and precipitation of Al-polymers and hydroxides onto various sheet silicates. They pointed out that although Al tends to adsorb in polymeric form onto kaolinite, gibbsite formation usually is prevented (Barnhisel and Rich, 1963; 1965). This has been called the "anti-gibbsite" effect and was first noted by Jackson in 1963 (as cited in Jardine and Zelazny, 1996). In contrast, gibbsite precipitation on basal planes of montmorillonite could be simulated easily in the laboratory on Wyoming bentonite (montmorillonite) (Turner and Brydon, 1965; Brydon and Kodama, 1966). Turner and Brydon (1967) demonstrated that if gibbsite formation on kaolinite is not prevented, it is at least slowed relative to gibbsite formation on illite or montmorillonite. They also proposed that gibbsite precipitation occurred on charged kaolinite edges rather than uncharged basal surfaces.

These observations suggest that in acidic to neutral solutions, gibbsite precipitates preferentially on basal surfaces of 2:1 layer silicates rather than the protonated edges of 2:1 layer silicates, and that on 1:1 layer silicates with no permanent charge, precipitation occurs preferentially on the protonated edges, although at a slower rate.

4.4. Reactive Versus Total Surface Area

Two lines of evidence suggest that once gibbsite nucleated on a substrate, further growth occurred primarily on the newly formed gibbsite surface rather than the substrate. The evidence includes (1) the similarity of growth rates when normalized to total gibbsite surface area or to the muscovite basal surface area, and (2) the crystal-cluster type of morphology. Gibbsite growth on muscovite occurred at a relatively high supersaturation and produced a variety of crystal morphologies. Crystal clusters suggest multiple nucleation sites in response to strain-induced defects arising from epitaxial nucleation of the initial crystals, other structural defects arising from the relatively fast growth rates, or twinning. Therefore, nucleation site density and nucleation rate are probably the most important factors in controlling the overall measured growth rates of gibbsite.

Gibbsite growth rates on kaolinite are brought closer to the curve for gibbsite growth on gibbsite only when a surface area equal to about 8% of the total measured BET surface area is used to normalize rates. Eight percent of the total BET surface area of kaolinite most likely corresponds to the amount of Al-octahedral sheet edges exposed. Sutheimer et al. (1999) measured the percentage of edge surface area from atomic force microscopy images of 170 grains of each of KGa1b and KGa2, well and poorly crystallized Georgia kaolinite standards from the Source Repository of The Clay Minerals Society. They obtained an average of 17–18% edge surface area for both kaolinites based on gross particle morphology. They estimated an additional 4–5% of edge surface area arising from small steps on the basal surfaces, for a maximum of ~22% edge surface area. Twiggs County, Georgia kaolinite is more similar to the KGa2 Clay Minerals Society standard kaolinite in grain size and total BET surface area (Nagy et al., 1991; Van Olphen and Fripiat, 1979). Assuming an average of 17.5% edge surface area for Twiggs Co., Georgia kaolinite, one-half of the edge surface, or 8.75% of the total surface area, would represent the aluminum octahedral sheet. This is close to our estimate of 8% reactive surface area for gibbsite growth on the kaolinite. One-half of 22% yields an Al-octahedral edge surface area of 11%, somewhat higher than our fitted surface area of 8%. Not all aluminol sites at the edges will be protonated at pH 3 (Cygan, 1998), so the 8% estimate of reactive surface area may be more indicative of the density of protonated aluminol sites rather than total aluminol sites. We assumed that the basal Al-octahedral and Si-tetrahedral surfaces would be relatively unreactive (e.g., Brady et al., 1996).

The results of Nagy and Lasaga (1993) also support the low estimate for kaolinite's reactive surface area. They measured gibbsite growth rates in mixed gibbsite and Twiggs Co., Georgia kaolinite substrates and assumed that gibbsite grew only on itself. Growth rates from their study normalized to the gibbsite seed surface area cluster on both sides of the fitted curve in Fig. 1. This suggests that adjustment of the rates in the mixed-substrate experiments by adding reactive kaolinite surface area to the surface area for gibbsite growth is warranted only if the area for gibbsite growth on kaolinite is small. Results of the present study support the assertion of Nagy and Lasaga (1993) that kaolinite is relatively unreactive with respect to gibbsite growth in the presence of gibbsite.

4.5. Measurement of Growth Rate Ex-situ Using AFM

The AFM has been used successfully to quantify in situ mineral dissolution and growth rates (e.g., Hillner et al., 1992; Gratz et al., 1993; Bosbach and Rammensee, 1993). This has been possible because step motion is fast enough to capture within the time scale of the imaging process for the ionically bonded phases studied (calcite and gypsum) (Dove and Platt, 1996). One requirement in measuring in-situ dissolution rates using AFM is that the mineral surface be relatively defect free. Typically, dissolution rates of salts as measured by ledge migration or etch pit formation are slower than rates measured in bulk powder experiments (Dove and Platt, 1996). Bulk rates for dissolution and growth of sheet silicates and some Al-hydroxides are at least three orders of magnitude slower (Nagy, 1995) than rates for calcite and gypsum and would be difficult to measure in situ without elevated temperature control. Therefore, ex situ measurements are more likely to yield quantitative rate information. To our knowledge, application of AFM imaging analysis software to quantify volumetrically the ex situ growth rates of minerals is new.

4.6. Saturation State of Solutions with Respect to the Substrate

Experimental solution compositions were both supersaturated with respect to gibbsite and undersaturated with respect to kaolinite and muscovite. We assumed that the dominant reaction at the surface was gibbsite precipitation. At 80°C our measured gibbsite precipitation rates are at least two orders of magnitude faster than muscovite dissolution rates [using 70°C data from Knauss and Wolery (1989) and assuming a doubling of rate at 80°C]. They are also one to two orders of magnitude faster than kaolinite dissolution rates (Carroll and Walther, 1990). Thus, the density of dissolution sites (e.g., etch pits nucleated at crystal defects or points of chemical impurities) on the muscovite surface in TMAFM images should be approximately 1% of the density of newly precipitated gibbsite crystals. If dissolution is faster at the muscovite edges than on the basal surface, the concentration of dissolution features in TMAFM images of the basal surfaces would be even lower. Although we did not observe randomly distributed etch features in our TMAFM images, we cannot rule out some nucleation of gibbsite crystallites at dissolution sites on the basal surface. Because the dissolution rates for both substrates are no greater than 1 to 10% of the gibbsite precipitation rates, dissolution sites on the substrate could control the nucleation of gibbsite if the average size of a gibbsite crystallite is 10 to 100 times that of the original dissolution site.

4.7. Implications for Modeling Reactive Surface Area in Natural Systems

Our major result is that heterogeneous nucleation and growth of gibbsite occurs by a likely epitaxial mechanism on surfaces of structurally similar phases under conditions of gibbsite supersaturation in the bulk fluid. Various nucleation and growth mechanisms of secondary phases on substrate minerals have been described in numerous recent spectroscopic studies (e.g., Hazemann et al., 1992; Charlet and Manceau, 1992, 1994; O'Day et al., 1994, 1996; Scheidegger et al., 1997, 1998) of

metal sorption onto mineral substrates. The secondary phase may have an epitaxial, topotactic, or no obvious structural relationship to the substrate. In these investigations, solutions may have been supersaturated in the interfacial region while maintaining undersaturation in the bulk phase away from the surface. However, formation of a structurally recognizable secondary precipitate requires supersaturation or at least equilibrium in the solution directly in contact with the secondary phase.

The concept of reactive surface area has been recognized universally as a major parameter yet to be characterized well in natural systems (e.g., Hochella and Banfield, 1995; Lichtner, 1996). Banfield and Barker (1994) stressed that during weathering, reactive surface area for the growth of clays is frequently interior to nonclay grains, and growth rates may be controlled by surface or grain boundary diffusion rather than surface-controlled reactions. Our investigation of precipitation of sheet-structured phases from bulk solution shows that crystal structure and surface charge density regulate the nucleation sites. Assuming that subsequent gibbsite growth on heterogeneous phases is controlled by precipitation on newly formed gibbsite surface area, nucleation site density is the variable that needs to be examined more closely when calculating growth in reactive-transport models.

Distribution of permanent structural and pH-dependent surface charge plus matching of structural geometries are probably the primary controls on precipitation of sheet-structured phases on other sheet-structured phases. If structures match perfectly as in the case of gibbsite growth on gibbsite, then the total BET surface area is reactive. If there is significant structural misfit to the nucleating phase, then the distribution of surface charge must be analyzed. For substrates lacking permanent charge, pH-dependent surface charge controls nucleation site density. For sheet silicates, pH-dependent charge is concentrated at edge surfaces, and hence edge surface area only may be reactive. For substrates with permanent charge, nucleation should be a function of both the permanent charge and pH-dependent charge densities, making both basal and edge surfaces, or in other words the total BET surface area, reactive.

5. CONCLUSIONS

The growth rate of gibbsite on gibbsite, kaolinite, and muscovite substrates at 80°C and pH3 can be expressed by a linear relation between rate and saturation state provided the surface area to which rates are normalized is adjusted to represent the probable location and concentration of reactive nucleation sites. Crystal nucleation and growth rates for gibbsite on the three substrates depend on a set of related geometric, surface charge, and solution saturation state effects. For example, kaolinite and muscovite appear to provide epitaxial templates for the growth of gibbsite, although epitaxy may occur only on the edges of kaolinite where there is pH-dependent surface charge, and on both the basal and edges surfaces of muscovite where there are permanent and pH-dependent charge, respectively. Further detailed investigation of the role of surface charge in controlling nucleation and growth is necessary.

Quantitative analysis of atomic force microscopy images to calculate crystal growth mass on a well-characterized flat surface has been applied for the first time as a new technique for measuring mineral growth rates. This technique could prove very useful for examining reactions close to equilibrium, and at the microscopic level at which direct comparison to synchrotron source x-ray absorption fine structure (XAFS) and x-ray scattering measurements of polynuclear precipitates can be made.

Finally, we conclude that the choice of nucleation substrates in reactive transport modeling must be modified. The idea that substrates should be modeled only as the same phase as the precipitate or as a metastable phase cannibalized during the formation of the precipitate is invalid. The presence of model nucleation substrates should truly represent the natural system. Use of an estimated surface area for growth should be made with some insight into the concentration and location of potential nucleation sites in the natural system. Our results offer an approach for improving the calculation of nucleation and growth kinetics in reactive transport models.

REFERENCES

Altschuler Z. S., Dwornik E. J., and Kramer H. (1963) Transformation of montmorillonite to kaolinite during weathering. *Science* **141,** 148–152.

Bailey S. W. (1984) Crystal chemistry of the true micas. In *Reviews in Mineralogy: Micas* (ed. S. W. Bailey), Vol. 13, Chap. 2, pp. 13–60. MSA.

Banfield J. F. and Barker W. W. (1994) Direct observation of reactant-product interfaces formed in natural weathering of exsolved, defective amphibole to smectite: Evidence for episodic, isovolumetric reactions involving structural inheritance. *Geochim. Cosmochim. Acta* **58,** 1419–1429.

Banfield J. F., Jones B. F., and Veblen D. R. (1991a) An AEM–TEM study of weathering and diagenesis, Abert lake, Oregon: I. Weathering reactions in the volcanics. *Geochim. Cosmochim. Acta* **55,** 2781–2793.

Banfield J. F., Jones B. F., and Veblen D. R. (1991b) An AEM–TEM study of weathering and diagenesis, Abert lake, Oregon: II. Diagenetic modification of the sedimentary assemblage. *Geochim. Cosmochim. Acta* **55,** 2795–2810.

Barker W. W. and Banfield J. F. (1996) Biologically versus inorganically mediated weathering reactions: Relationships between minerals and extracellular microbial polymers in lithobiontic communities. *Chem. Geol.* **132,** 55–69.

Barnhisel R. I. (1969) Changes in specific surface areas of clays treated with hydroxy-aluminum. *Soil Sci.* **107,** 126–130.

Barnhisel R. I. and Rich C. I. (1963) Gibbsite formation from aluminum-interlayers in montmorillonite. *Soil Sci. Soc. Amer. Proc.* **27,** 632–635.

Barnhisel R. I. and Rich C. I. (1965) Gibbsite, bayerite, and nordstrandite formation as affected by anions, pH, and mineral surfaces. *Soil Sci. Soc. Amer. Proc.* **29,** 531–534.

Bates R. G. (1973) *Determination of pH, Theory and Practice*. Wiley.

Boles J. R. and Johnson K. S. (1983) Influence of mica surfaces on pore-water pH. *Chem. Geol.* **43,** 303–317.

Bosbach D. and Rammensee W. (1994) In situ investigation of growth

and dissolution on the (010) surface of gypsum by Scanning Force Microscopy. *Geochim. Cosmochim. Acta* **58,** 843–849.

Bottero J. Y., Axelos M., Tchoubar D., Cases J. M., Fripiat J. J., and Fiessinger F. (1987) Mechanism of formation of aluminum trihydroxide from Keggin Al$_{13}$ polymers. *J. Colloid Interface Sci.* **117,** 47–57.

Brady P. V., Cygan R. T., and Nagy K. L. (1996) Molecular controls on kaolinite surface charge. *J. Colloid Interface Sci.* **183,** 356–364.

Brydon J. E. and Kodama H. (1966) The nature of aluminum hydroxide-montmorillonite complexes. *Amer. Mineral.* **51,** 875–889.

Burch T. E., Nagy K. L., and Lasaga A. C. (1993) Free energy dependence of albite dissolution kinetics at 80°C and pH 8.8. *Chem. Geol.* **105,** 137–162.

Burns A. F. and White J. L. (1963) Removal of potassium alters b-dimension of muscovite. *Science* **139,** 39–40.

Burton W. K., Cabrera N., and Frank F. C. (1951) The growth of crystals and the equilibrium structure of their surfaces: *Philos. Trans. R. Soc. London, Ser. A* **243,** 299–358.

Carroll S. A. and Walther J. W. (1990) Kaolinite dissolution at 25°, 60°, and 80°C. *Amer. J. Sci.* **290,** 797–810.

Carroll-Webb S. A. and Walther J. V. (1988) A surface complex reaction model for the pH-dependence of corundum and kaolinite dissolution rates. *Geochim. Cosmochim. Acta* **52,** 1545–1556.

Charlet L. and Manceau A. (1992) X-ray absorption spectroscopic study of the sorption of Cr(III) at the oxide/water interface. II Adsorption, coprecipitation and surface precipitation on ferric hydrous oxides. *J. Colloid Interface Sci.* **148,** 425–442.

Charlet L. and Manceau A. (1994) Evidence for the neoformation of clays upon sorption of Co(II) and Ni(II) on silicates. *Geochim. Cosmochim. Acta* **58,** 2577–2582.

Chiarello R. P. and Sturchio N. C. (1994) Epitaxial growth of otavite on calcite observed in situ by synchrotron X-ray scattering. *Geochim. Cosmochim. Acta* **58,** 5633–5638.

Collins D. R. and Catlow C. R. A. (1990) Interatomic potentials for micas. *Mol. Sim.* **4,** 341–346.

Crowley S. F. (1991) Diagenetic modification of detrital muscovite: An example from the Great Limestone Cyclothem (Carboniferous) of Co. Durham, UK. *Clay Miner.* **26,** 91–103.

Cygan R. T. (1998) Molecular models of metal sorption on clay minerals. In *CMS Workshop Lectures, Molecular Modeling of Clays and Mineral Surfaces* (eds. J. D. Kubicki and W. F. Bleam), Vol. 10. Chap. 4. CMS, in press.

Dove P. M. and Platt F. M. (1996) Compatible real-time rates of mineral dissolution by Atomic Force Microscopy (AFM). *Chem. Geol.* **127,** 331–338.

Fortin D., Ferris F. G., and Beveridge T. J. (1997) Surface-mediated mineral development by bacteria. In *Reviews in Mineralogy: Geomicrobiology: Interactions between Microbes and Minerals* (eds. J. F. Banfield and K. H. Nealson), Vol. 35, Chap. 5, pp. 161–180. MSA.

Giese R. F. Jr. (1988) Kaolin minerals: Structures and stabilities. In *Reviews in Mineralogy: Hydrous Phyllosilicates* (ed. S. W. Bailey), Vol. 19, Chap. 3, pp. 29–66. MSA.

Gratz A. J., Hillner P. E., and Hansma P. K. (1993) Step dynamics and spiral growth on calcite. *Geochim. Cosmochim. Acta* **57,** 491–495.

Hanchar J. M., Nagy K. L., Fenter P., Finch R. J., Beno D. J., and Sturchio N. C. (1999) Quantification of minor phases in growth kinetics experiments with powder X-ray diffraction. *Amer. Mineral.* (to be published).

Harsh J. B., Doner H. E., and McBride M. B. (1984) Chemisorption of copper on hydroxy-aluminum-hectorite: An electron spin resonance study. *Clays Clay Miner.* **32,** 407–413.

Hazemann J. L., Manceau A., Sainctavit Ph., and Malange C. (1992) Structure of the αFe$_x$Al$_{1-x}$OOH solid solution I. Evidence by polarized EXAFS for an epitaxial growth of hematite-like clusters in Fe-diaspore. *Phys. Chem. Miner.* **19,** 25–38.

Hillner P. E., Gratz A. J., Manne S., and Hansma P. K. (1992) Atomic-scale imaging of calcite growth and dissolution in real time. *Geology* **20,** 359–362.

Hochella M. F. Jr. and Banfield J. F. (1995) Chemical weathering of silicates in nature: A microscopic perspective with theoretical considerations. In *Reviews in Mineralogy: Chemical Weathering Rates of Silicate Minerals* (eds. A. F. White and S. L. Brantley), Vol. 31. Chap. 8, pp. 353–406. MSA.

Hu J., Xiao X.-D., Ogletree D. F., and Salmeron M. (1995) The structure of molecularly thin films of water on mica in humid environments. *Surf. Sci.* **344,** 221–236.

Jardine P. M. and Zelazny L. W. (1996) Surface reaction of aqueous aluminum species. In *The Environmental Chemistry of Aluminum* (ed. G. Sposito), Chap. 6, pp. 221–270. CRC.

Johnsson P. A., Hochella M. F. Jr., Parks G. A., Blum A. E., and Sposito G. (1992) Direct observation of muscovite basal-plane dissolution and secondary phase formation: An XPS, LEED, and SFM study. In *Water-Rock Interaction* (eds. Y. K. Kharaka and A. S. Maest). Vol. 7, pp. 159–162. A. A. Balkema, Rotterdam.

Knauss K. G. and Wolery T. J. (1989) Muscovite dissolution kinetics as a function of pH and time at 70°C. *Geochim. Cosmochim. Acta* **53,** 1493–1502.

Lichtner P. C. (1996) Continuum formulation of multicomponent-multiphase reactive transport. *In Reviews in Mineralogy: Reactive Transport in Porous Media* (eds. P. C. Lichtner, C. I. Steefel, and E. H. Oelkers), Vol. 34, Chap. 1, pp. 1–81. MSA.

Lichtner P. C., Steefel C. I., and Oelkers E. H. (1996) Reactive Transport in Porous Media. In *Reviews in Mineralogy*, Vol. 34. MSA.

Merino E., Nahon D., and Wang Y. (1993) Kinetics and mass transfer of pseudomorphic replacement: Application to replacement of parent minerals and kaolinite by Al, Fe, and Mn oxides during weathering. *Amer. J. Sci.* **293,** 135–155.

Muller J.-P., Manceau A., Calas G., Allard T., Ildefonse, P., and Hazemann J.-L. (1995) Crystal chemistry of kaolinite and Fe-Mn oxides: relation with formation conditions of low temperature systems. *Amer. J. Sci.* **295,** 1115–1155.

Nagy K. L. (1995) Dissolution and precipitation kinetics of sheet silicates. In *Reviews in Mineralogy: Chemical Weathering Rates of Silicate Minerals* (eds. A. F. White and S. L. Brantley), Vol. 31, Chap. 5, pp. 173–233. MSA.

Nagy K. L. and Lasaga A. C. (1992) Dissolution and precipitation kinetics of gibbsite at 80°C and pH3: The dependence on solution saturation state. *Geochim. Cosmochim. Acta* **56,** 3093–3111.

Nagy K. L. and Lasaga A. C. (1993) Simultaneous precipitation kinetics of kaolinite and gibbsite at 80°C and pH3. *Geochim. Cosmochim. Acta* **57,** 4329–4335.

Nagy K. L., Blum A. E., and Lasaga A. C. (1991) Dissolution and precipitation kinetics of kaolinite at 80°C and pH3: The dependence on solution saturation state. *Amer. J. Sci.* **291,** 649–686.

Nugent M. A., Brantley S. L., Pantano C., and Maurice P. A. (1998) The influence of natural mineral coatings on feldspar weathering. *Nature* **395,** 588–591.

O'Day P. A., Brown G. E. Jr., and Parks G. A. (1994) X-ray absorption spectroscopy of cobalt(II) multinuclear surface complexes and surface precipitates on kaolinite. *J. Colloid Interface Sci.* **165,** 269–289.

Odelius M., Bernasconi M., and Parrinello M. (1997) Two dimensional ice adsorbed on mica surface. *Phys. Rev. Lett.* **78,** 2855–2858.

Ohara M. and Reid R. C. (1973) *Modeling Crystal Growth Rates from Solution.* Prentice-Hall.

Palmer D. A. and Wesolowski D. J. (1992) Aluminum speciation and equilibria in aqueous solution. Part II. the solubility of gibbsite in acidic sodium chloride solutions from 30 to 70°C. *Geochim. Cosmochim. Acta* **56,** 1093–1111.

Pevear D. R., Klimentidis R. E., and Robinson G. A. (1991) Petrogenetic significance of kaolinite nucleation and growth on pre-existing mica in sandstones and shales. 28th Annual Meeting of the Clay Minerals Society, 125 (abstr.).

Pokrovskii V. A. and Helgeson H. C. (1995) Thermodynamic properties of aqueous species and the solubilities of minerals at high pressures and temperatures: the system Al$_2$O$_3$-H$_2$O-NaCl. *Amer. J. Sci.* **295,** 1255–1342.

Radoslovich E. W. and Norrish K. (1962) The cell dimensions and symmetry of layer-lattice silicates. *Amer. Mineral.* **47,** 599–616.

Scheidegger A. M., Lamble G. M., and Sparks D. L. (1997) Spectroscopic evidence for the formation of mixed-cation hydroxide phases upon metal sorption on clays and aluminum oxides. *J. Colloid Interface Sci.* **186,** 118–128.

Scheidegger A. M., Strawn D. G., Lamble G. M., and Sparks D. L. (1998) The kinetics of mixed Ni-Al hydroxide formation on clays

and aluminum oxides: A time-resolved XAFS study. *Geochim. Cosmochim. Acta* **62,** 2233–2245.

Smith R. W. and Hem J. D. (1972) Effect of aging on aluminum hydroxide complexes in dilute aqueous solutions. U.S. Geological Survey Water-Supply Paper 1827-D.

Smyth J. R., Dyar M. D., May H. M., Bricker O. P., and Acker J. G. (1997) Crystal structure refinement and Mossbauer spectroscopy of an ordered, triclinic clinochlore. *Clays Clay Miner.* **45,** 544–550.

Steefel C. I. and Van Cappellen P. (1990) A new kinetic approach to modeling water-rock interaction: The role of nucleation, precursors, and Ostwald ripening. *Geochim. Cosmochim. Acta* **54,** 2657–2677.

Sutheimer S., Maurice P., and Zhou Q. (1999) Dissolution of well and poorly crystallized kaolinites: Al speciation and effects of surface characteristics. *Amer. Miner.,* in press.

Sverjensky D. A. (1994) Zero-point-of-charge prediction from crystal chemistry and solvation theory. *Geochim. Cosmochim. Acta* **58,** 3123–3129.

Taylor R. M. (1987) Non-silicate oxides and hydroxides. In *Chemistry of Clays and Clay Minerals* (ed. A. C. D. Newman). Mineralogical Society Monograph No. 6, pp. 129–201.

Teng H. H., Dove P. M., Orme C. A., and De Yoreo J. J. (1998) Thermodynamics of calcite growth: Baseline for understanding biomineral formation. *Science* **282,** 724–727.

Tosi M. P. (1964) Cohesion of ionic solids in the Born model. *Solid State Phys.* **16,** 1–120.

Turner R. C. and Brydon J. E. (1965) Factors affecting the solubility of $Al(OH)_3$ precipitated in the presence of montmorillonite. *Soil Sci.* **100,** 176–181.

Turner R. C. and Brydon J. E. (1967) Effect of length of time of reaction on some properties of suspensions of Arizona bentonite, illite, and kaolinite in which aluminum hydroxide is precipitated. *Soil Sci.* **103,** 111–117.

Van Olphen H. and Fripiat J. J. (1979) *Data Handbook for Clay Materials and other Non-metallic Minerals*. Pergamon.

Veesler S. and Boistelle R. (1994) Growth kinetics of hydrargillite $Al(OH)_3$ from caustic soda solutions. *J. Crystal Growth* **142,** 177–183.

Wesolowski D. J. (1992) Aluminum speciation and equilibria in aqueous solution: I. the solubility of gibbsite in the system Na-K-Cl-OH-$Al(OH)_4$ from 0 to 100°C. *Geochim. Cosmochim. Acta* **56,** 1065–1091.

White A. F. and Peterson M. L. (1990) Role of reactive-surface-area characterization in geochemical kinetic models. In *Chemical Modeling of Aqueous Systems II*. (eds. D. C. Melchior and R. L. Bassett). ACS Symposium Series 416, Chap. 35, pp. 461–475. ACS.